



## Original Research

## Hierarchically porous biochar derived from aerobic granular sludge for high-performance membrane capacitive deionization

Yurong Zhang<sup>a</sup>, Xudong Bu<sup>a,\*</sup>, Yajun Wang<sup>a</sup>, Zhenyu Hang<sup>b</sup>, Zhiqiang Chen<sup>a,c,\*\*</sup><sup>a</sup> School of Civil Engineering, Lanzhou University of Technology, Lanzhou, 730050, China<sup>b</sup> Shaanxi Key Laboratory of Environmental Engineering, Xi'an University of Architecture and Technology, Xi'an, 710055, China<sup>c</sup> State Key Laboratory of Urban Water Resource and Environment, Harbin Institute of Technology (SKLUWRE, HIT), Harbin, 150090, China

## ARTICLE INFO

## Article history:

Received 27 December 2022

Received in revised form

2 July 2023

Accepted 5 July 2023

## Keywords:

Membrane capacitive deionization

Desalination

Aerobic granular sludge

Biochar

Alkali activation

## ABSTRACT

Membrane capacitive deionization (MCDI) is a cost-effective desalination technique known for its low energy consumption. The performance of MCDI cells relies on the properties of electrode materials. Activated carbon is the most widely used electrode material. However, the capacitive carbon available on the market is often expensive. Here, we developed hierarchically porous biochar by combining carbonization and activation processes, using easily acquired aerobic granular sludge (AGS) from biological sewage treatment plants as a precursor. The biochar had a specific surface area of  $1822.07 \text{ m}^2 \text{ g}^{-1}$ , with a micropore area ratio of 58.65% and a micropore volume of  $0.576 \text{ cm}^3 \text{ g}^{-1}$ . The MCDI cell employing the biochar as electrodes demonstrated a specific adsorption capacity of  $34.35 \text{ mg g}^{-1}$ , comparable to commercially available activated carbon electrodes. Our study presents a green and sustainable approach for preparing highly efficient, hierarchically porous biochar from AGS, offering great potential for enhanced performance in MCDI applications.

© 2023 Published by Elsevier B.V. on behalf of Chinese Society for Environmental Sciences, Harbin Institute of Technology, Chinese Research Academy of Environmental Sciences. This is an open access article under the CC BY-NC-ND license (<http://creativecommons.org/licenses/by-nc-nd/4.0/>).

## 1. Introduction

Population growth and economic development have increased the demand for fresh water. To meet this increasing demand, researchers have focused on developing high-efficiency desalination technology for obtaining clean water from seawater or brackish water. Conventional desalination methods, such as reverse osmosis, electrodialysis, and multistage flash distillation, have been widely used; however, these methods consume high amounts of energy and cause secondary pollution. Capacitive deionization (CDI) is a promising alternative to these conventional methods owing to its inherent features, such as easy operation, low energy footprint, and environmental friendliness [1–4]. In this method, voltage is applied to the electrodes, during which ionic species from the feed water stream are immobilized due to charge compensation, causing the desalination of brine. However, the co-ion expulsion effect limits the desalination capacity and charge efficiency of the CDI cell. To

promote desalination, membrane capacitive deionization (MCDI) cells are developed by introducing cation and anion exchange membranes between two porous carbon electrodes [5,6]. The intrinsic characteristics of these electrode materials considerably affect the desalination performance of MCDI cells.

MCDI cells can be further developed using various electrode materials with different electrochemical desalination mechanisms, such as capacitor-like and battery-like electrodes. Although intercalation and redox materials offer high desalination efficiency, carbon-based materials are used as electrodes for hybrid architectures in MCDI cells. This is primarily because these materials are electrochemically stable, and their electrode potential is within the electrochemical stability window of aqueous electrolytes [7,8]. Moreover, carbon-based materials have a wide range of sources, good chemical stability, and tunable structure properties. Activated carbon (AC), carbon nanotubes, carbon nanofibers, carbon aerogels, and graphene are commonly used carbon-based electrode materials in MCDI cells. AC is particularly promising owing to its low cost, simple synthesis, and environmental friendliness [9–11]. AC electrode materials have a hierarchically porous structure and offer large capacitance and specific surface area for the electroadsorption of salts in MCDI cells, ensuring their wide applicability. Thus, green

\* Corresponding author.

\*\* Corresponding author. School of Civil Engineering, Lanzhou University of Technology, Lanzhou, 730050, China.

E-mail addresses: [buxd@lut.edu.cn](mailto:buxd@lut.edu.cn) (X. Bu), [cqzhit@163.com](mailto:cqzhit@163.com) (Z. Chen).

and sustainable methods must be developed for synthesizing AC electrode materials.

Municipal wastewater treatment plants generate activated sludge as the main byproduct from the secondary sedimentation tank during biological wastewater treatment. The sludge mainly comprises microorganisms inhabiting in the activated sludge, hard-to-degrade organic solids, N, P, and K nutrients accumulated by microbial metabolism, pathogenic bacteria, and heavy metals. Treatment of 10000 tons of wastewater generates 5–10 tons of sludge, with a water content of 80%. Such a high yield of sludge will comprise >50% of pollutants in sewage, including various heavy metals, trace amounts of highly toxic organic substances, and a large number of pathogenic microorganisms, posing a great threat to the ecological environment. If the sludge is not appropriately treated, it will cause damage to the water environment and soil and eventually threaten drinking water and food safety. To this end, sludge treatment and disposal methods are proposed for harmless and resourceful treatment of sludge [12–14]. In such methods, the sludge is thickened, dewatered, stabilized, and dried. It is then reused and recycled via landfilling and incineration. Sludge incineration is the most promising sludge treatment and disposal method owing to its small carbon footprint, high treatment efficiency, and excellent recovery of thermal energy and inorganic resources of ash; however, the treatment cost is high, and the resource utilization of incinerator ash is poor. This method also causes secondary pollution [13,15,16].

Aerobic granular sludge (AGS), a new wastewater treatment solution, has higher microbial activity and aggregation and a unique granular structure than conventional activated sludge [17,18]. Herein, hierarchically porous biochar was prepared for high-performance MCDI using AGS as the precursor for the first time. Biochar stabilizes the pollutants in sludge and uses AC for pollutant removal, thus realizing wastewater treatment [19,20]. Compared with the sludge obtained from traditional sewage wastewater treatment plants, AGS has a dense, porous granular structure due to the special aggregation mode of microorganisms. Microbial aggregation primarily depends on the microbial extracellular polymeric substance (EPS); the high content of polysaccharides and polyproteins in EPS enables AGS to have a higher carbon content per unit mass [21]. Herein, a hierarchically porous biochar with a high specific surface area was prepared by combining carbonization and activation processes using AGS as the precursor. Using the as-prepared biochar, a model MCDI cell was constructed that exhibited higher specific adsorption capacity, higher charge efficiency, and lower energy consumption compared with commercial AC electrodes. The results of this study will promote green development by reducing carbon footprint and emissions during sludge treatment and provide new pathways to obtaining high-performance porous carbon electrodes for MCDI.

## 2. Materials and methods

### 2.1. Preparation of biochar

AGS used as the precursor for developing hierarchically porous biochar (Fig. 1) was obtained from the sludge discharged from a wastewater treatment system under laboratory conditions that used a sequencing batch reactor (SBR). The sludge was collected starting from the 143rd day of SBR operation until the 153rd day, and during this stage the sludge was mainly in the form of particles. The granular sludge was cultivated mainly using nutrients, chemical oxygen demand, and ammonia nitrogen (Fig. 1a). Then, the supernatant was sieved, and the as-obtained sludge was dried in an oven at 80 °C for 6 h to remove moisture (Fig. 1b). The dried sludge was then pre-carbonized at different temperatures of 400, 500, and

600 °C in Ar atmosphere for 2 h at a heating rate of 5 °C min<sup>-1</sup>. After carbonization, the obtained product was mixed with KOH at mass ratios of 1:1, 1:2, and 1:3, followed by alkali activation at 800 °C for 1 h at a heating rate of 10 °C min<sup>-1</sup> in Ar atmosphere. Subsequently, the samples were washed with 2 M hydrochloric acid and deionized water about 3–5 times until it reached a neutral pH. The final product was dried overnight in an oven at 80 °C. The carbonization and activation yields were calculated using the mass of the product obtained after carbonization divided by the mass of the dried sludge and the mass of material after alkali activation divided by the mass of the product obtained after carbonization. The total yield was calculated using the product of the two. The samples obtained (Fig. 1c) by carbonization at 400, 500, and 600 °C and activation with KOH at a mass ratio of 1:2 were denoted as BC-400, BC-500, and BC-600, respectively. The samples obtained by carbonization at 400 °C and activation with KOH at mass ratios of 1:1, 1:2, and 1:3 were denoted as 400-BC-1, 400-BC-2, and 400-BC-3.

### 2.2. Characterization

The thermogravimetric behavior of AGS was studied by thermogravimetric analysis (TGA, STA449F3). The morphological features of the samples were investigated by field emission scanning electron microscopy (FESEM, JSM 6701F). The specific surface area and pore size distribution of the samples were analyzed by nitrogen adsorption–desorption isotherms obtained using Micromeritics ASAP 2000. X-ray diffraction (XRD) measurements were performed using the Rigaku D/Max-2400 diffractometer to determine the crystallographic information and crystalline phases of the samples. Raman analysis was performed using a high-resolution Raman spectrometer (HORIBA Jobin Yvon SAS, France) to understand the sample structure. X-ray photoelectron spectroscopy (XPS) was performed using a Thermo Scientific K-Alpha+ spectrometer with Al K $\alpha$  radiation (1486.6 eV) on the powdered samples pressed into a thin slice. Fourier transform infrared spectroscopy (FT-IR, Bruker ALPHA) was used to characterize the molecular structure of the surface functional groups. Elemental analysis of the samples was performed using SEM and energy dispersive spectroscopy (EDS, JSM-5601LV), mainly for C, N, P, S, and heavy metals.

### 2.3. Electrochemical measurements

Electrodes were prepared by homogeneously mixing 80 wt% of biochar, 10 wt% of acetylene black, and 10 wt% of polyvinylidene fluoride (PVDF) binder. Then, the slurry was pressed at 10 MPa on a stainless-steel grid current collector and dried in a vacuum oven at 80 °C for 12 h. Electrochemical measurements were performed on an electrochemical workstation (DH7000, Donghua, China) at room temperature in 1 M sodium chloride electrolyte with an active material loading of 1 mg. Cyclic voltammetry (CV), galvanostatic charge–discharge (GCD), and electrochemical impedance spectroscopy (EIS) tests were conducted in a three-electrode system with Pt sheet and saturated calomel (Hg<sub>2</sub>Cl<sub>2</sub>/KCl) as the counter and reference electrodes, respectively. EIS measurements were performed at a frequency of 0.01–100 kHz with an amplitude of 5 mV. CV and GCD tests were first cycled 10 times to ensure a steady state of the system before recording; the measurements were then performed at –0.6–0.3 V. The electrochemically active surface areas (ECSAs) of the electrodes were determined from their double-layer capacitance ( $C_{dl}$ ). Cyclic voltammograms were obtained in a non-Faradaic region from –0.2 to –0.1 V [22–24]. The potential of zero charges ( $E_{pzc}$ ) of samples was tested using the CV curves at 1 mV s<sup>-1</sup> in 5 mM NaCl solution. The specific capacitance  $C$  (F g<sup>-1</sup>) of the active materials was calculated from the cyclic voltammograms and GCD curves using equations (1) and (2):

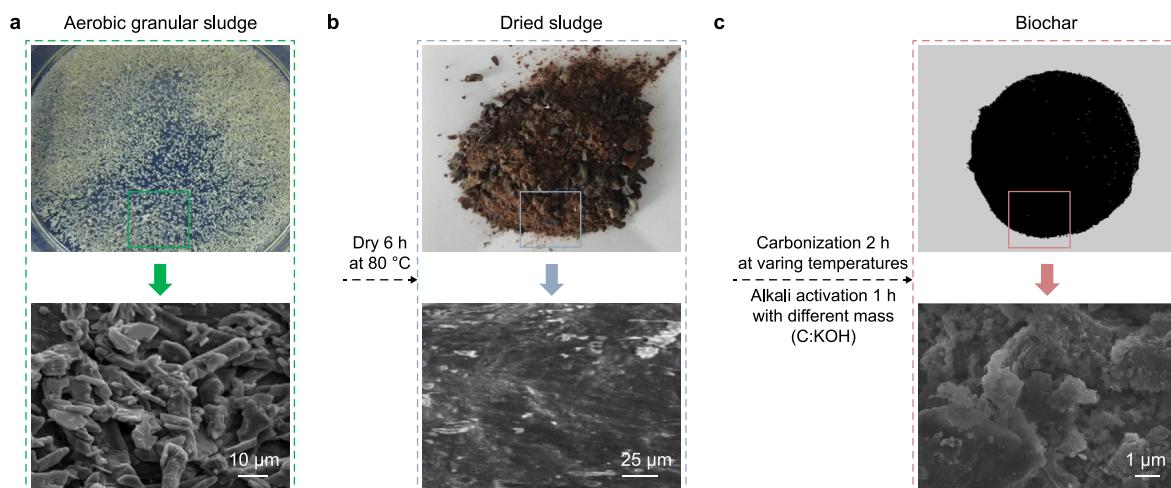


**Fig. 1.** a, AGS collected from the drainage of an AGS wastewater treatment system. b, The sludge was obtained after 6 h of drying at 80 °C. c, The biochar is obtained by carbonization and activation.

$$C = \int_{V_1}^{V_2} \frac{I dV}{2mv} \quad (1)$$

$$C = \frac{I \Delta t}{m \Delta V} \quad (2)$$

where  $I$  (A) is the load current,  $\Delta V$  (V) is the test voltage window,  $\Delta t$  (s) is the discharge time corresponding to the specified potential change  $\Delta V$ ,  $m$  (g) is the total mass loading of the active material, and  $v$  ( $V s^{-1}$ ) is the scan rate. The electrochemical stability of the samples was determined by installing a symmetrical button supercapacitor on a blue electric workstation (LANHE, CT3002A). Long-cycling stability tests were performed using galvanostatic charge–discharge cycles at a voltage range of 0–1.2 V and  $0.25 A g^{-1}$  in 20 mM NaCl solution.

#### 2.4. MCDI desalination performance tests

A laboratory-scale CDI cell was assembled using two electrodes of 3-cm diameter with a coating mass loading of  $4 mg cm^{-2}$  (Fig. 2a). The two electrodes were separated by a silicone gasket to form a single channel with a 2-mm spacing, known as the desalting channel. Anion exchange membranes (AEMs, AMI-7001, USA) and cation exchange membranes (CEMs, CMI-7001, USA) were placed on the anode and cathode electrode surfaces of the CDI cell, respectively (Fig. 2b). Details of the ion exchange membranes are shown in Table S1. Commercial AC-based desalination cells were fabricated using the same method used for biochar-based cells.

An electrochemical workstation (DH7000, Donghua, China) was

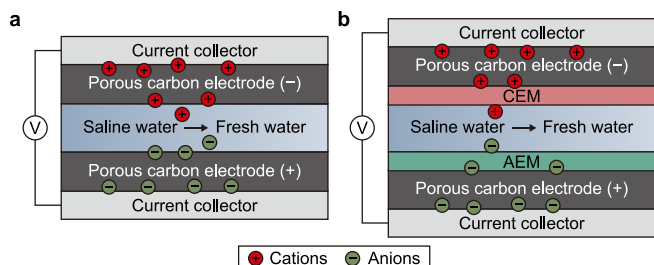


**Fig. 2.** Schematic of the CDI (a) and MCDI (b) architecture using the prepared biochar.

used as a potentiost for power supply; it recorded the changes in current in different batches. 15 mL of 20 mM NaCl solution was continuously circulated through the desalting channel using a peristaltic pump at a flow rate of  $6 mL min^{-1}$ . The electrodes were charged at a constant voltage of 1.2 V for 30 min until the adsorption reached a dynamic equilibrium and then continuously discharged at a reverse voltage of  $-1.2 V$  for 30 min to regenerate the electrodes. The change in conductivity was recorded using an online water quality analysis meter (DZS-708, Leici, China). The specific adsorption capacity (SAC,  $mg g^{-1}$ ), charge efficiency ( $\Delta charge$ , %), and energy consumption ( $E_m$ ,  $kJ mol^{-1}$ ) required to remove a unit mole of salt (NaCl) were used as the evaluation indicators of desalination performance and calculated using following equations: [25,26].

$$SAC = \frac{(C_{feed} - C_{effluent})V}{m} \quad (3)$$

where  $V$  (L) is the treated water volume,  $C_{feed}$  and  $C_{effluent}$  ( $mg L^{-1}$ ) is the measured mass concentration,  $m$  (mg) is the total mass of the positive and negative active materials.

$$\Delta charge = \frac{F(C_{feed} - C_{effluent})V}{M(NaCl)Q_{in}(C)} \quad (4)$$

where  $M(NaCl)$  is the molar mass of NaCl  $58.5 g mol^{-1}$ ,  $F$  is Faraday constant  $96458 C mol^{-1}$ ,  $Q_{in}$  (C) is the input charge during the charging process.

$$E_m = \frac{\int_0^{t_{charge}} iU dt}{(C_{feed} - C_{effluent})VM(NaCl)} \quad (5)$$

where  $i$  (A) is the charging current,  $U$  (V) is the working voltage,  $t_{charge}$  (s) is the corresponding charging time.

### 3. Results and discussion

#### 3.1. Properties of AGS

AGS, used as the precursor, was derived from the sludge generated from a sewage treatment plant. Sludge was collected

continuously during the smooth operation of the treatment plant; heterotrophic denitrifiers were also formed during the process. The average concentration of mixed liquor suspended solid (MLSS) in the SBR reactor was  $3613 \pm 70 \text{ mg L}^{-1}$ , and the average MLSS concentration in the sludge was  $170 \pm 57.66 \text{ mg L}^{-1}$ . Meanwhile, the sedimentation ratios at 5 min and 30 min were  $SV_5 = 29 \pm 1.49\%$  and  $SV_{30} = 20.9 \pm 0.74\%$ , which indicate that the particles have a dense structure. The particle size distribution curves are shown in Fig. 3a and b, wherein  $dp_i$  is the percentage of the number of particles with a particle size  $d_i$ , and  $p_i$  is the percentage of all particles with a particle size less than  $d_i$ . The average particle size distribution increases from 138.52 to 334.78  $\mu\text{m}$ , with an obvious peak at 99.76  $\mu\text{m}$ , indicating an increase in the particle size and the continuous formation of new particles in the SBR. The discharge sludge coagulates to form particles, proving its feasibility to be used as the AGS.

AGS primarily contains C, O, N, P, and S, as indicated using EDS (Fig. 3c); 50.0% of convertible carbon was present in the AGS, an important indicator of biomass precursor. The higher carbon content is due to the presence of bacterial EPS. The oxygen and nitrogen contents are 38.7% and 9.4%, respectively. The rich carbon, oxygen, and nitrogen contents are related to the high microbial aggregation characteristics of AGS. The microstructures of particles of different sizes in the sludge were investigated by SEM. Large particles ( $>500 \mu\text{m}$ ) have a denser structure because of the dense aggregation of rod-shaped bacteria (Fig. 3d,j), medium particles (200–500  $\mu\text{m}$ ) show a clear agglomeration of bacteria (Fig. 3e,h),

and small particles ( $<200 \mu\text{m}$ ) have a loose alum flower-like structure (Fig. 3f,i). These rod-shaped bacteria further promoted inter-bacterial agglomeration by EPS. The resulting AGS had a higher carbon content because EPS is primarily composed of sugar and proteins. Thus, the inherent characteristics, such as high carbon content, high porosity, and a porous matrix of AGS, are favorable for preparing porous carbon electrodes [27].

### 3.2. Characteristics of biochar

The hierarchically porous biochar was fabricated from AGS by combining carbonization and activation processes. The carbonization temperatures and activation methods influence the biochar characteristics [28,29]. Nitrogen absorption–desorption and pore size distribution characterizations were performed on the samples, as shown in Fig. S1. Table 1 lists the pore characteristics of the samples. The sample prepared by carbonization at 400 °C and alkali activation with KOH at a mass ratio of 1:2 (400-BC-2) had the largest Brunauer–Emmett–Teller surface area ( $S_{\text{BET}}$ ) of  $1822.07 \text{ m}^2 \text{ g}^{-1}$ . Moreover, 400-BC-2 exhibited a hierarchical microporous and mesoporous structure, with a micropore area ratio of 58.65% and a micropore volume of  $0.576 \text{ cm}^3 \text{ g}^{-1}$ . The specific surface area decreased with increasing carbonization temperature. To further explore AGS decomposition, TGA was performed at 25–850 °C (Fig. S2). The weight loss of samples at 80–105 °C was 1.17%, which is attributed to the loss of physically bound water. The weight loss of samples at 105–400 °C was about

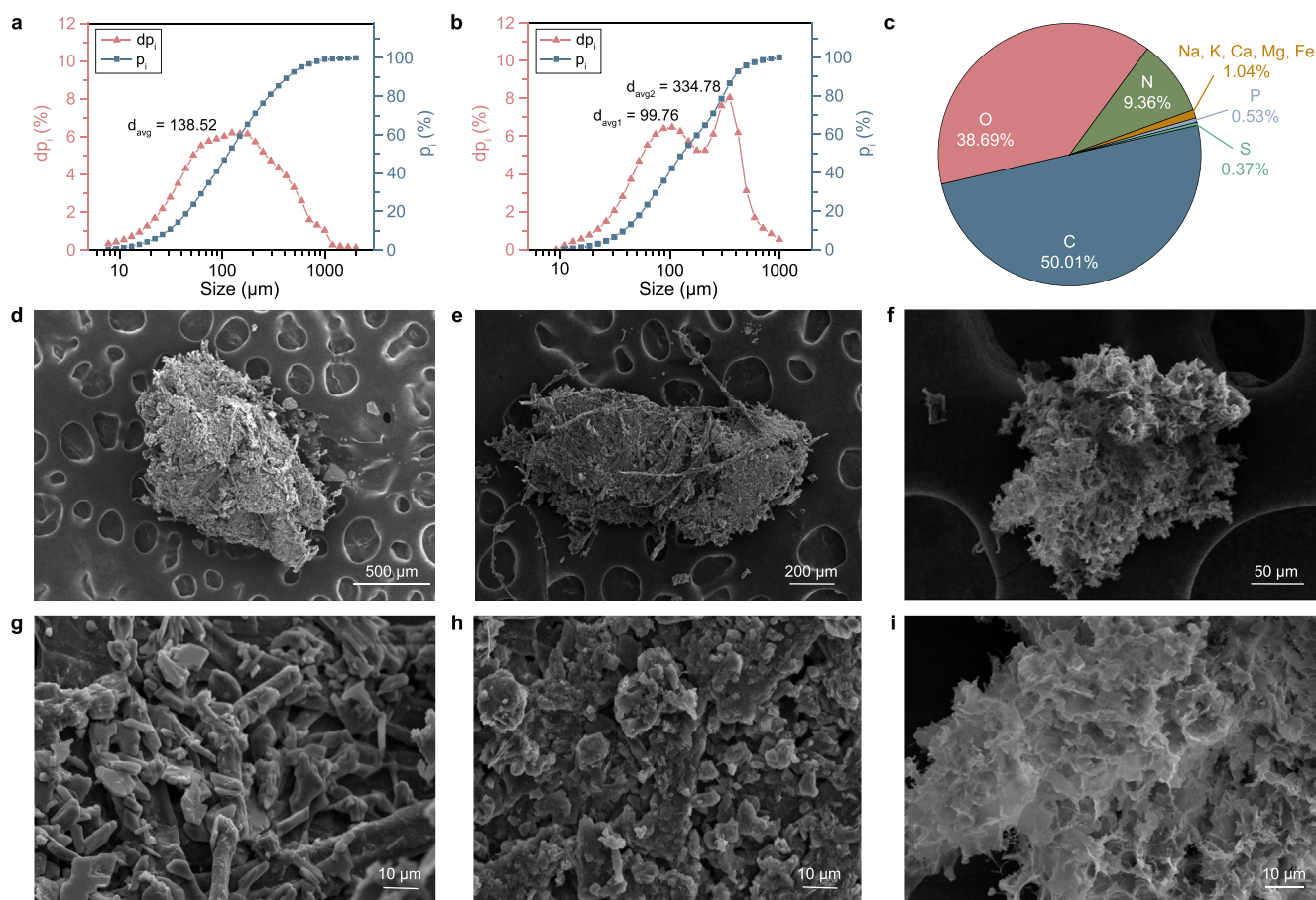


**Fig. 3.** a–b, AGS particle size distribution at the beginning of sludge collection (day 143, a) and at the end (day 153, b). c, Elemental composition of the dried sludge obtained from EDS. d, g, SEM images of large particles in the collected sludge with low (d) and high (g) magnifications. e, h, SEM images of medium particles in the collected sludge with low (e) and high (h) magnifications. f, i, SEM images of small particles in the collected sludge with low (f) and high (i) magnifications.

**Table 1**  
Summary of the pore characterization and carbonization/activation yield of the biochar samples.

Samples	$S_{\text{BET}}$ ( $\text{m}^2 \text{g}^{-1}$ )	Micropore area ( $\text{m}^2 \text{g}^{-1}$ )	Micropore area ratio (%)	Total pore volume ( $\text{cm}^3 \text{g}^{-1}$ )	Micropore volume ratio (%)	Carbonization yield (%)	Activation yield (%)	Total yield (%)
BC-400/400-BC-2	1822.07	1068.66	58.65	1.098	52.46	43.81	29.67	13
BC-500	1268.27	558.54	44.04	0.996	30.52	34.97	33.48	11.71
BC-600	984.15	623.01	63.30	0.635	52.89	32.81	45.32	14.87
400-BC-1	1256.89	884.29	70.36	0.851	55.11	43.81	48.16	21.10
400-BC-3	938.38	631.51	67.30	0.686	48.98	43.81	13.99	6.12
PCT-21	1618.23	1020.39	63.06	0.863	63.04	Commercial		

55%, which can be attributed to the decomposition of organic materials, such as EPS, bacteria, biodegradable substances, and semivolatile matter. This weight loss increased the specific surface area and number of micropores in the sample. Macromolecules, such as humic matter, were decomposed between 400 and 580 °C, reducing the specific surface area and the number of micropores.

During activation, KOH reacted with carbon to form micropores in the samples [30,31]. The alkali activation with KOH at a mass ratio of 1:2 is considered optimal because plugged pores are removed, and carbon porosity is increased under this condition. Moreover, a mass ratio of 1:1 is insufficient for effective activation, and a higher mass ratio (1:3) can lead to excessive etching and reduce the effective carbon content, thereby decreasing the specific surface area and pore volume. The effects of carbonization temperature and alkali activation on the biochar properties can be further analyzed based on the biochar yields obtained under different carbonization and alkali activation conditions. Higher biochar yields were obtained at lower carbonization temperatures; however, the corresponding alkali activation yield was lower. Herein, the total biochar yield was 13% under optimal processing conditions, carbonization temperature of 400 °C, and alkali activation with KOH at a mass ratio of 1:2.

Compared with the as-prepared biochar, the commercial AC, PCT-21 (Shandong Obo New Material Co., Ltd), has a smaller  $S_{\text{BET}}$  of 1618.23  $\text{m}^2 \text{g}^{-1}$  and a micropore-specific surface area of 63.06%. Nitrogen adsorption-desorption isotherms and hysteresis loops (Fig. 4a) show that BC-400-2 has a type-II isotherm and a pronounced hysteresis loop, which reveals its typical microporous/mesoporous structure [32]. PCT-21, on the contrary, has a type-I isotherm and microporous structure. The pore size of 400-BC-2 is concentrated in two regions of 1–2 and 2–50 nm, in which the micropore and mesopore volumes account for about 50%. The pore size distribution of PCT-21 is mainly concentrated in the 1–3-nm region (Fig. 4b). The nitrogen adsorption-desorption isotherms of the remaining biochar samples revealed hierarchical microporous/mesoporous carbons (Fig. S1b), and smaller adsorption amounts than BC-400-2. BC-400-3 shows an H3-type hysteresis loop in the high relative pressure  $P/P_0$  region, with the characteristics of cracks; this indicates that a high alkali mass ratio would damage the microporous structure of biochar. According to the principle of electric double layers (EDLs), AC with a large specific surface area usually has better capacitive performance. Thus, 400-BC-2 will have electrochemical performance comparable to PCT-21.

The sample structures were analyzed by XRD (Fig. 4c and S3). All the samples exhibited two broad diffraction peaks at around 23° and 43°, which were assigned to the (002) and (100) planes [33]; no other impurity peaks were observed. Raman spectra revealed that the samples have two obvious peaks at 1361 and 1591  $\text{cm}^{-1}$  (Fig. 4d), which are the D peak (due to the stretching motion of non- $\text{sp}^2$  atom pairs; defects) and G peak (stretching motion of  $\text{sp}^2$  atoms; graphitization) [34]. The ratios of integrated areas of the D and G peaks ( $I_{\text{D}}/I_{\text{G}}$ ) are 1.43 and 1.27 for 400-BC-2 and PCT-21,

respectively.  $I_{\text{D}}/I_{\text{G}}$  ratios decreased with increasing carbonization temperature and alkali mass ratio (Fig. S4), indicating more defects in the 400-BC-2 than in the other biochar samples. XPS was performed to test the structural defects in the sample. The full spectrum verified the presence of C, O, and N (Fig. 4e). The high-resolution profile of C1s exhibited four peaks with binding energies of 284.2, 285.1, 286.10, and 288.50 eV, which corresponded to C–C ( $\text{sp}^2$ ), C–O/C–N, “defective peak” ( $\text{sp}^3$ ), and C=O, respectively (Fig. 4f) [19,20]. In particular, the presence of the C- $\text{sp}^3$  configuration indicates that the carbon is intrinsically defective. The intrinsic defects serve as active sites for ion adsorption and induce the local charge density rearrangement of carbon groups for improving the ion adsorption capacity. In addition, the peaks of N1s at 398.5, 399.9, and 401.7 eV correspond to pyridinic-N, pyrrolic-N, and graphitic-N, respectively (Fig. 4g) [21]. The defective sites produced by pyridinic-N and pyrrolic-N can enhance the electronic conductivity of carbon and improve the ion storage performance [22].

The results of the surface functional groups of the samples characterized by FT-IR are shown in Fig. 4h. The functional groups of the AGS were the most abundant, corresponding to the C–H bending and stretching vibrations at 1434 and 2922–2943, respectively, and C=C functional group at 1572–1658  $\text{cm}^{-1}$ . The peaks located at 3460 and 1730  $\text{cm}^{-1}$  corresponded to the –OH and C=O functional groups [35]. In contrast, 400-BC-2 and PCT-21 only showed weak C–O peaks at 1024–1074  $\text{cm}^{-1}$ ; therein, intensive peaks were observed for the other samples (Fig. S5). These results are inconsistent with the  $E_{\text{pzc}}$  test results obtained by CV at 1  $\text{mV s}^{-1}$  in 5 mM NaCl solution (Fig. S6), with  $E_{\text{pzc}}$  of 0.19 and 0.12 V for 400-BC-2 and PCT-21, respectively [36]. Oxygen-containing functional groups make the surface negatively charged; this is not conducive to the desalination performance of CDI anodes [37]. SEM was used to observe the morphological characteristics of 400-BC-2 (Fig. S7), which visibly revealed its rough surface and numerous microporous channels; thus, it is more conducive to providing adsorption sites. These characteristics are mainly due to the porous structure, and the characteristics of the AGS used as the precursor. The elemental composition of 400-BC-2 was analyzed by EDS, as shown in Fig. 4i; the carbon content reached 92.1%, and the oxygen content was only 6.6%. Moreover, no heavy metal buildup was noted, thus confirming its applicability as a CDI electrode.

### 3.3. Electrochemical performance

To validate the advantages of the 400-BC-2 electrode, the electrochemical performances of as-prepared AC and PCT-21 electrodes were compared in a three-electrode system in 1 M NaCl solution. Typical cyclic voltammograms at different scan rates and GCD curves at different current densities were recorded (Fig. S8). Fig. 5a shows the representative cyclic voltammograms of 400-BC-2 and PCT-21 electrodes at a scan rate of 5  $\text{mV s}^{-1}$ . The cyclic voltammograms of both electrodes are nearly rectangular, demonstrating an excellent characteristic of EDL performance [38]. The GCD curves

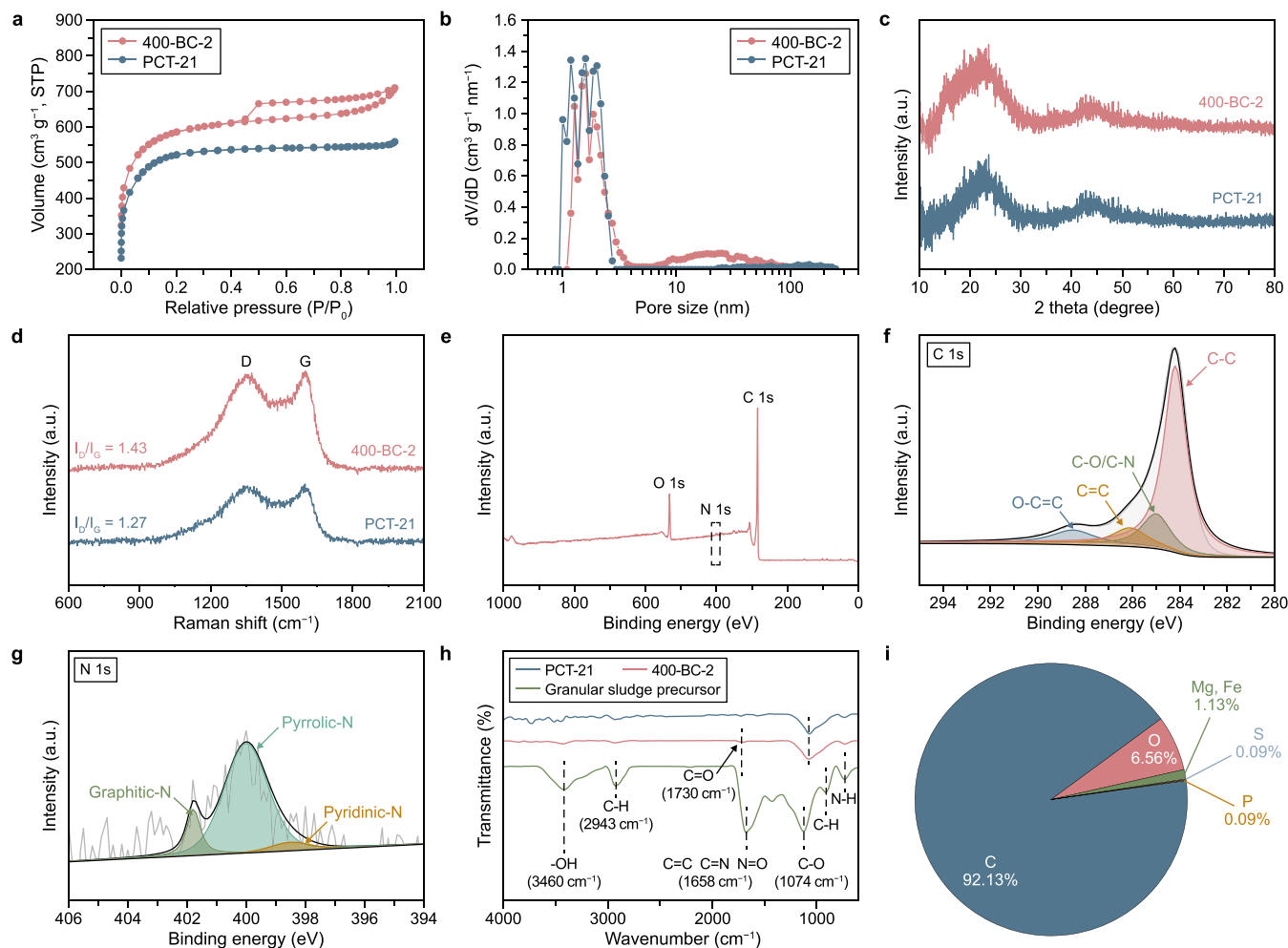


**Fig. 4.** a–d, Nitrogen adsorption–desorption isotherms (a), pore size distribution curves (b), XRD patterns (c), and Raman spectra (d) of 400-BC-2 and PCT-21. e, XPS full spectrum of 400-BC-2. f–g, High-resolution C 1s (f) and N 1s (g) spectra. h, FT-IR spectra of 400-BC-2 and PCT-21. i, Elemental composition of 400-BC-2.

at different current densities showed characteristic symmetrical triangular profiles (Fig. S8). 400-BC-2 showed a larger integral area than PCT-21. As plotted in Fig. 5b, the specific capacitance of 400-BC-2 is 8–16%, higher than that of PCT-21. EIS plots (Fig. 5c) further showed that 400-BC-2 had lower equivalent series resistance and ion transport resistance. Such advantages were mainly attributed to the larger surface area, better pore size distribution, and special surface structure of 400-BC-2. The cyclic voltammograms and GCD curves of the as-prepared AC electrodes (Fig. S8) were used to compare the specific capacitances at different scan rates and current densities (Fig. S9). The specific capacitances decreased for all samples as the sweep speed increased and showed a positive correlation between specific capacitance and specific surface area. Notably, ECSA is an effective method to assess the actual ion-accessible surface in the electrochemical test [24]. The results show that the 400-BC-2 electrode exhibited the most significant ECSA (Figs. S10 and 11), consistent with the previously reported electrochemical test results in a three-electrode system. To further evaluate the reversibility and stability of the as-prepared AC, a BC-400-2 symmetric supercapacitor coin cell was assembled. In the long-cycling stability test of the coin cell, after 10000 cycles at a current density of  $0.25 \text{ A g}^{-1}$  in 20 mM NaCl electrolyte, the capacitance remained almost constant, and the Coulombic efficiency was ~100% (Fig. 5d).

### 3.4. MCDI performance

To further explore the desalination properties of BC-400-2, CDI, and MCDI cells were experimentally assembled for desalination tests. Fig. 6a shows the current profiles obtained at an operation voltage of 1.2 V. When an external voltage was applied, the effluent concentration gradually decreased to an approximately constant value after 30 min, indicating that ions were adsorbed onto the surface of the AC electrodes and dynamic equilibrium was achieved. When a reverse external voltage of  $-1.2 \text{ V}$  was applied, the effluent concentration gradually returned to its initial value, revealing that the ions were released from the AC electrode surface (Fig. 6b). The effluent concentration obtained for the CDI cell showed similar trend to that obtained for the MCDI cell (Fig. S12). When the dynamic equilibrium was achieved, compared with the PCT-21 electrode, the BC-400-2 electrode exhibited a lower effluent concentration and adsorbed a larger amount of salt, showing a higher specific capacity. The results agreed well with the previous results obtained from the three-electrode system test (Fig. 5).

EIS curves further provided impedance and diffusion limits for different desalination cells (Fig. 6c). In the CDI cells, small charge transfer resistances were revealed, as negligible circle radius in the high frequency region. And the BC-400-2 electrode showed a more

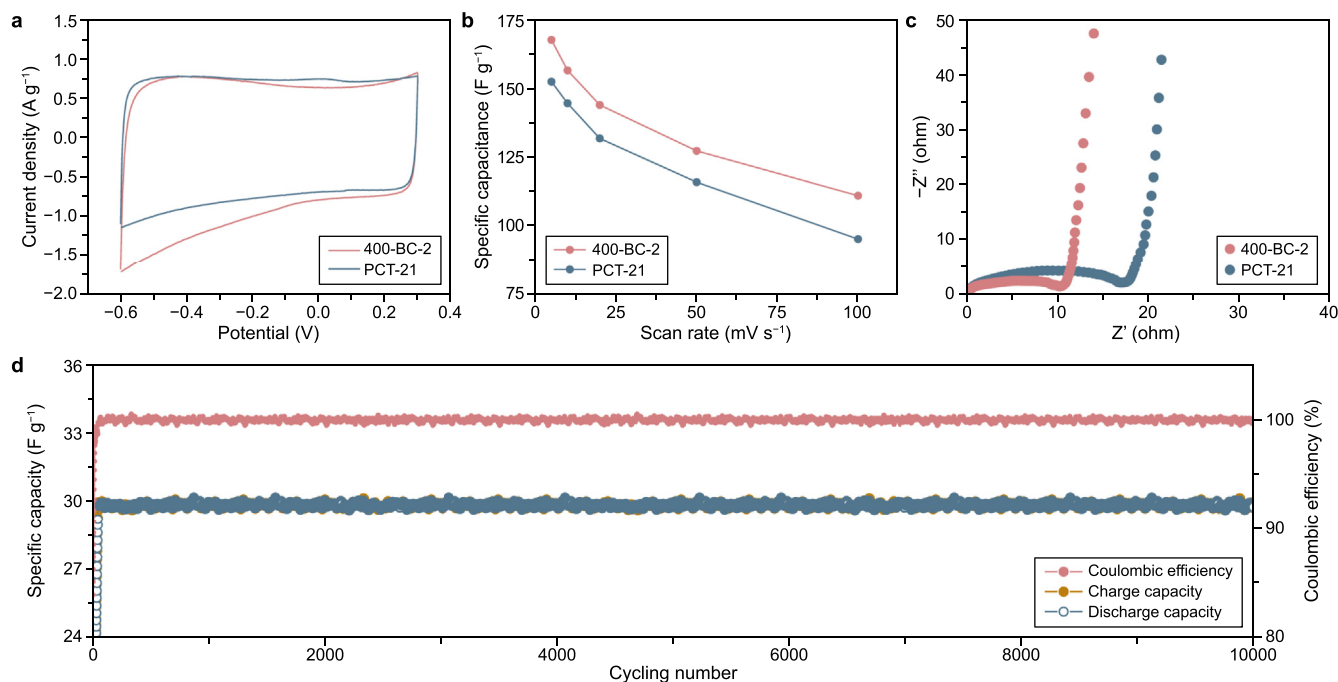


**Fig. 5.** a, The cyclic voltammograms at a scan rate of 5 mV s<sup>-1</sup> b, specific capacitances at different scan rates ranging from 5 to 100 mV s<sup>-1</sup> c, Nyquist plots of the 400-BC-2 and PCT-21 electrodes in 1 M NaCl solution using three-electrode system. d, Cyclic performance of the BC-400-2 symmetric supercapacitor.

obvious capacitive behavior, as the EIS has a large linear slope in the low frequency region, which is close to vertical. With the addition of AEM and CEM, the internal resistance of the MCDI cell increased, but capacitive behavior remained. Fig. 6d shows the SAC, charge efficiency, and  $E_m$  of different desalination cells.

membranes significantly improve the charge efficiency and SAC of MCDI compared to the CDI cell [39]. The SAC of the BC-400-2 electrode in the MCDI cell (34.35 mg g<sup>-1</sup>) is about three times that of the electrode in the CDI cell (11.21 mg g<sup>-1</sup>). The charge efficiency increased from 36.63% to 96.9%, and the corresponding

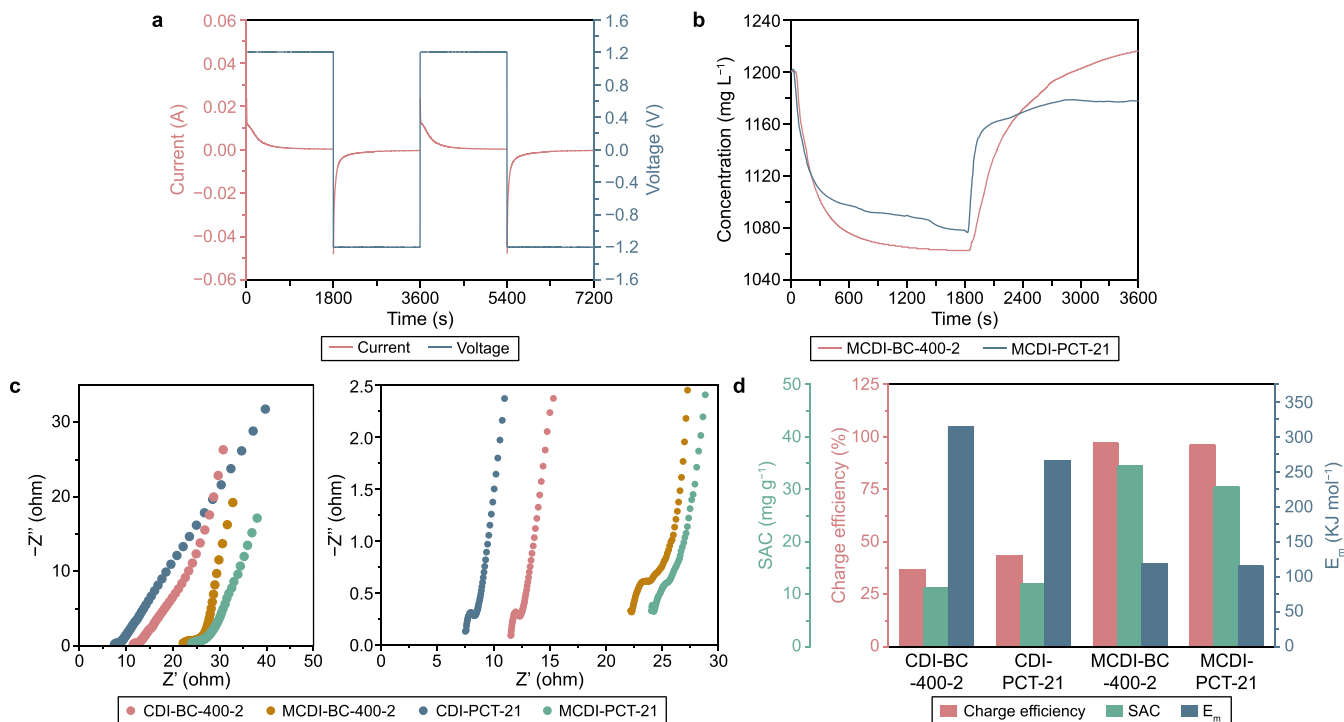


**Fig. 6.** Representative desalination performance of the MCDI cell. a, Current and voltage profiles during operation. b, Variation curves of the effluent concentration with time in one cycle. c–d, Comparison of EIS (c), and SAC, charge efficiency, and  $E_m$  of different desalination cells (d). For panel c, the right figure is an enlarged version of the left.

energy consumption  $E_m$  required for removing unit mol of NaCl decreased to  $118.68 \text{ kJ mol}^{-1}$ , which was only 37.79% of that for the CDI cell. In contrast, the SAC of the MCDI cell using the BC-400-2 electrode was higher than that using the PCT-21 cell, which can be further verified using Ragone plots (Fig. S13) [40,41]. Thus, the superior performance of BC-400-2 makes it a potential electrode for practical applications.

#### 4. Conclusions

Hierarchical porous biochar was successfully prepared by combining carbonization and activation using AGS as the precursor. AGS has high carbon content and porosity. Upon carbonization at  $400^\circ\text{C}$  and alkali activation with KOH at a mass ratio of 1:2, the prepared biochar had a specific surface area of  $1822.07 \text{ m}^2 \text{ g}^{-1}$  and a hierarchical microporous and mesoporous structure. Electrochemical performance tests showed that biochar had a specific capacitance of  $167.87 \text{ F g}^{-1}$  at  $5 \text{ mV s}^{-1}$ , 12% higher than that of PCT-21. The as-prepared biochar is a promising candidate electrode for the MCDI cell. Results showed that the MCDI cell based on the prepared biochar exhibited a desalination performance comparable to the commercial AC PCT-21. The carbonization of AGS to synthesize biochar solves the issue of sludge disposal in sewage treatment plants and provides a simple and environmentally friendly method for preparing green and low-cost carbon materials for MCDI.

#### CRedit authorship contribution statement

**Yurong Zhang:** Investigation, Writing - Original Draft. **Xudong Bu:** Methodology, Writing - Review & Editing. **Yajun Wang:** Project Administration. **Zhenyu Hang:** Data Curation. **Zhiqiang Chen:** Supervision, Funding Acquisition.

#### Declaration of competing interest

The authors declare that they have no known competing financial interests or personal relationships that could have appeared to influence the work reported in this paper.

#### Acknowledgements

We gratefully acknowledge financial support from the National Natural Science Foundation of China (Grant No. 52160003 and 52264039), the State Key Laboratory of Urban Water Resource and Environment at Harbin Institute of Technology (2020DX05), Natural Science Foundation of Gansu Province (Grant No.20JR5RA436), the National Key Research & Development Program of China (2022YFC3203101), and Foster Foundation of International Research Base of Seismic Mitigation and Isolation of Gansu Province (No. GII2022-P02).

#### Appendix A. Supplementary data

Supplementary data to this article can be found online at <https://doi.org/10.1016/j.ese.2023.100297>.

#### References

- [1] P. Srimuk, X. Su, J. Yoon, D. Aurbach, V. Presser, Charge-transfer materials for electrochemical water desalination, ion separation and the recovery of elements, *Nat. Rev. Mater.* 5 (7) (2020) 517–538.
- [2] J.G. Gamaethiralalage, K. Singh, S. Sahin, J. Yoon, M. Elimelech, M.E. Suss, P. Liang, P.M. Biesheuvel, R.L. Zornitta, L.C.P.M. de Smet, Recent advances in ion selectivity with capacitive deionization, *Energy Environ. Sci.* 14 (3) (2021) 1095–1120.

- [3] J. Ma, P. Liang, X. Sun, H. Zhang, Y. Bian, F. Yang, J. Bai, Q. Gong, X. Huang, Energy recovery from the flow-electrode capacitive deionization, *J. Power Sources* 421 (6) (2019) 50–55.
- [4] S. Xu, T. Wang, C. Wang, C. Chen, C. Dong, C.P. Huang, The effect of crystal phase of manganese oxide on the capacitive deionization of simple electrolytes, *Sci. Total Environ.* 675 (2019) 31–40.
- [5] R. Zhao, P.M. Biesheuvel, A. van der Wal, Energy consumption and constant current operation in membrane capacitive deionization, *Energy Environ. Sci.* 5 (11) (2012) 9520–9527.
- [6] W. Tang, D. He, C. Zhang, P. Kovalsky, T.D. Waite, Comparison of Faradaic reactions in capacitive deionization (CDI) and membrane capacitive deionization (MCDI) water treatment processes, *Water Res.* 120 (2017) 229–237.
- [7] J. Lee, S. Kim, C. Kim, J. Yoon, Hybrid capacitive deionization to enhance the desalination performance of capacitive techniques, *Energy Environ. Sci.* 7 (11) (2014) 3683–3689.
- [8] L. Gao, Q. Dong, S. Bai, S. Liang, C. Hu, J. Qiu, Graphene oxide-tuned MoS<sub>2</sub> with an expanded interlayer for efficient hybrid capacitive deionization, *ACS Sustainable Chem. Eng.* 8 (26) (2020) 9690–9697.
- [9] M.S. Gaikwad, C. Balomajumder, Tea waste biomass activated carbon electrode for simultaneous removal of Cr(VI) and fluoride by capacitive deionization, *Chemosphere* 184 (2017) 1141–1149.
- [10] X.T. Xu, H.M. Tang, M. Wang, Y. Liu, Y.J. Li, T. Lu, L.K. Pan, Carbon spheres with hierarchical micro/mesopores for water desalination by capacitive deionization, *J. Mater. Chem.* 4 (41) (2016) 16094–16100.
- [11] X. Liu, J. Wang, Electro-assisted adsorption of Cs(I) and Co(II) from aqueous solution by capacitive deionization with activated carbon cloth/graphene oxide composite electrode, *Sci. Total Environ.* 749 (2020) 141524.
- [12] Y. Chen, R. Wang, X. Duan, S. Wang, N. Ren, S.H. Ho, Production, properties, and catalytic applications of sludge derived biochar for environmental remediation, *Water Res.* 187 (2020) 116390.
- [13] A. Raheem, V.S. Sikarwar, J. He, W. Dastyar, D.D. Dionysiou, W. Wang, M. Zhao, Opportunities and challenges in sustainable treatment and resource reuse of sewage sludge: a review, *Chem. Eng. J.* 337 (2018) 616–641.
- [14] M.C. Samolada, A.A. Zabaniotou, Comparative assessment of municipal sewage sludge incineration, gasification and pyrolysis for a sustainable sludge-to-energy management in Greece, *Waste Manage. (Tucson, Ariz.)* 34 (2) (2014) 411–420.
- [15] Y. Liang, D. Xu, P. Feng, B. Hao, Y. Guo, S. Wang, J.J. Klemes, Municipal sewage sludge incineration and its air pollution control, *J. Clean. Prod.* 295 (2021) 126456.
- [16] G. Yang, G. Zhang, H. Wang, Current state of sludge production, management, treatment and disposal in China, *Water Res.* 78 (2015) 60–73.
- [17] Y.V. Nancharaiyah, G.K.K. Reddy, Aerobic granular sludge technology: mechanisms of granulation and biotechnological applications, *Bioresour. Technol.* 247 (2018) 1128–1143.
- [18] M. Pronk, M.K. de Kreuk, B. de Bruin, P. Kamminga, R. Kleerebezem, M.C.M. van Loosdrecht, Full scale performance of the aerobic granular sludge process for sewage treatment, *Water Res.* 84 (2015) 207–217.
- [19] L.Y. Li, X. Gong, O. Abida, Waste-to-resources: exploratory surface modification of sludge-based activated carbon by nitric acid for heavy metal adsorption, *Waste Manage. (Tucson, Ariz.)* 87 (2019) 375–386.
- [20] B.A. Mohamed, L.Y. Li, H. Hamid, M. Jeronimo, Sludge-based activated carbon and its application in the removal of perfluoroalkyl substances: a feasible approach towards a circular economy, *Chemosphere* 294 (2022) 133707.
- [21] T. Peng, Y. Wang, J. Wang, F. Fang, P. Yan, Z. Liu, Effect of different forms and components of EPS on sludge aggregation during granulation process of aerobic granular sludge, *Chemosphere* 303 (2022) 135116.
- [22] V.C. Hoang, V.G. Gomes, K.N. Dinh, Ni- and P-doped carbon from waste biomass: a sustainable multifunctional electrode for oxygen reduction, oxygen evolution and hydrogen evolution reactions, *Electrochim. Acta* 314 (2019) 49–60.
- [23] Y.-H. Tang, S.-H. Liu, D.C.W. Tsang, Microwave-assisted production of CO<sub>2</sub>-activated biochar from sugarcane bagasse for electrochemical desalination, *J. Hazard Mater.* 383 (2020) 121192.
- [24] S. Huo, W. Ni, X. Song, M. Zhang, H. Wang, K. Li, Insight from the synergistic effect of dopant and defect interplay in carbons for high-performance capacitive deionization, *Sep. Purif. Technol.* 281 (2022) 119807.
- [25] G. Bharath, K. Rambabu, F. Banat, A. Hai, A.F. Arangadi, N. Ponpandian, Enhanced electrochemical performances of peanut shell derived activated carbon and its Fe<sub>3</sub>O<sub>4</sub> nanocomposites for capacitive deionization of Cr(VI) ions, *Sci. Total Environ.* 691 (2019) 713–726.
- [26] H. Jiang, J. Zhang, K. Luo, W. Xing, J. Du, Y. Dong, X. Li, W. Tang, Effective fluoride removal from brackish groundwaters by flow-electrode capacitive deionization (FCDI) under a continuous-flow mode, *Sci. Total Environ.* 804 (2022) 150166.
- [27] Z. Li, Y. Zhang, X. Wang, Air drying process of granules and characteristics of their structure, *Chin. J. Environ. Sci.* 32 (8) (2011) 2353–2357.
- [28] M. Gao, W.-K. Wang, Y.-M. Zheng, Q.-B. Zhao, H.-Q. Yu, Hierarchically porous biochar for supercapacitor and electrochemical H<sub>2</sub>O<sub>2</sub> production, *Chem. Eng. J.* 402 (2020) 126171.
- [29] G.A. Yakaboylu, C. Jiang, T. Yumak, J.W. Zondlo, J. Wang, E.M. Sabolsky, Engineered hierarchical porous carbons for supercapacitor applications through chemical pretreatment and activation of biomass precursors, *Renew. Energy* 163 (2021) 276–287.
- [30] K. Li, D. Zhang, X. Niu, H. Guo, Y. Yu, Z. Tang, Z. Lin, M. Fu, Insights into CO<sub>2</sub>

- adsorption on KOH-activated biochars derived from the mixed sewage sludge and pine sawdust, *Sci. Total Environ.* 826 (2022) 154133.
- [31] A. Zielińska, P. Oleszczuk, B. Charnas, J. Skubiszewska-Zięba, S. Pasieczna-Patkowska, Effect of sewage sludge properties on the biochar characteristic, *J. Anal. Appl. Pyrolysis* 112 (2015) 201–213.
- [32] H. Li, Z. Cheng, Q. Zhang, A. Natan, Y. Yang, D. Cao, H. Zhu, Bacterial-derived, compressible, and hierarchical porous carbon for high-performance potassium-ion batteries, *Nano Lett.* 18 (11) (2018) 7407–7413.
- [33] S. Liu, Y. Tang, Hierarchically porous biocarbons prepared by microwave-aided carbonization and activation for capacitive deionization, *J. Electroanal. Chem.* 878 (2020) 114587.
- [34] N. Environmental Science and Ecotechnology, X. Gu Wu, S. Zhou, X. Han, H. Leng, P. Zhang, P. Yang, Y. Qi, S. Li, J. Qiu, Hierarchical porous N, S co-doped carbon derived from fish scales for enhanced membrane capacitive deionization, *Electrochim. Acta* 409 (2022) 139983.
- [35] M. Boota, K.B. Hatzell, M. Alhabeab, E.C. Kumbur, Y. Gogotsi, Graphene-containing flowable electrodes for capacitive energy storage, *Carbon* 92 (2015) 142–149.
- [36] S. Duan, Y. Zhao, S. Jiang, Z. Yang, Y. Ju, C. Chen, L. Huang, F. Chen, Potential of zero charge regulating highly selective removal of nitrate anions through capacitive deionization, *Chem. Eng. J.* 442 (2022) 136287.
- [37] T. Wu, G. Wang, F. Zhan, Q. Dong, Q. Ren, J. Wang, J. Qiu, Surface-treated carbon electrodes with modified potential of zero charge for capacitive deionization, *Water Res.* 93 (2016) 30–37.
- [38] O. Sufiani, J. Elisadiki, R.L. Machunda, Y.A.C. Jande, Modification strategies to enhance electrosorption performance of activated carbon electrodes for capacitive deionization applications, *J. Electroanal. Chem.* 848 (2019) 113328.
- [39] Y.J. Kim, J.H. Choi, Improvement of desalination efficiency in capacitive deionization using a carbon electrode coated with an ion-exchange polymer, *Water Res.* 44 (3) (2010) 990–996.
- [40] W. Dianbudyanto, S.-H. Liu, Outstanding performance of capacitive deionization by a hierarchically porous 3D architectural graphene, *Desalination* 468 (2019) 114069.
- [41] T. Kim, J. Yoon, CDI ragone plot as a functional tool to evaluate desalination performance in capacitive deionization, *RSC Adv.* 5 (2) (2015) 1456–1461.